Applied Surface Science 393 (2017) 60–66

Contents lists available at ScienceDirect

Applied Surface Science

journal homepage: www.elsevier.com/locate/apsusc

Full Length Article

Carbon nanohoops as attractive toughening and lubricant agents in TiN porous films

Jianyun Zheng[a,c,*,1], Xiaodong Ren[b,1], Junying Hao[a,**], Ang Li[b], Weimin Liu[a]

[a] State Key Laboratory of Solid Lubrication, Lanzhou Institute of Chemical Physics, Chinese Academy of Sciences, Lanzhou 730000, China
[b] State Key Laboratory of Functional Materials for Informatics and Shanghai Center for Superconductivity, Shanghai Institute of Microsystem and Information Technology, Chinese Academy of Sciences, Shanghai 200050, China
[c] Qingdao Center of Resource Chemistry and New Materials, Qingdao 266000, China

ARTICLE INFO

Article history:
Received 17 July 2016
Received in revised form 7 September 2016
Accepted 29 September 2016
Available online 30 September 2016

Keywords:
Carbon nanohoops
TiN porous films
CH_4 plasma treatment
Modifying properties

ABSTRACT

Hoop-shaped conjugated macrocycles (or carbon nanohoops) are eliciting significant interest from theoretical and synthetic scientists on account of their eminent physical and chemical properties. Herein, carbon nanohoops firstly fabricated by CH_4 plasma treatment serve as toughening and lubricant agents in TiN porous films. The formation mechanism of carbon nanohoops is explained through a tandem Suzuki coupling/macrocyclization sequence of the charged multiple hydrocarbon molecules. The essential features of carbon nanohoops ensure that the TiN porous films with carbon nanohoops successfully possess flexible, hard, lubricant and antiwear effects.

1. Introduction

Carbon nanohoops are hoop-shaped π-conjugated molecules, in which paraphenylene units are linked in a cyclic manner [1]. Recently, the carbon nanohoops have been synthesized for applying in photo-, electro-, and photoelectronic fields because they are the simplest structural unit of armchair carbon nanotubes (CNTs) [2–4]. In fact, except functional properties, CNTs have been suggested ultra-high elastic modulus approaching 1 TPa, and exceptional tensile strengths in the range of 20–100 GPa [5,6]. CNT toughened materials can be achieved through crack deflection, crack bridging and CNT pull-out, for instance, in Al_2O_3 matrix [7]. Unfortunately, nanotube toughened thin films are yet to be realized due to difficulties in controlled alignment, interface reaction and reasonable volume fractions. Based on small volume, simple structure and similar properties, it is audaciously hypothesized that the films containing the carbon nanohoops will show a unique mechanical property.

Although carbon nanohoops have a simple structure, their synthesis has been a significant challenge [8,9]. After extensive efforts, some chemical researchers have reported innovative synthetic routes to prepare carbon nanohoops [10,11]. However, in these cases, the synthesis of carbon nanohoops involves the use of organic reagents with phenyl (e.g. cyclohexadiene), which can eventually produce additional pollutants. The need for a synthesis route without organic reagents stimulates the ongoing research in this field.

Titanium nitride (TiN) as a hard material is omnipresent in everyday life and plays a crucial role in multifarious engineering and functional applications. But the toughness and tribological behaviors of TiN hardly meet the demands of flexible devices and the micro-electro-mechanical systems [12]. Thus, in this work, we report the carbon nanohoops grown by CH_4 plasma treatment at room temperature with free organic reagents. The carbon nanohoops that are employed as toughening and lubricant agents are filled into the porous TiN film and cover the film surface to obtain a composite multilayer film (named as CTF). Compared with individual TiN porous films (TF, its preparation and structure shown in Supporting information (SI)), CTF can perform quadruple effects: flexible, hard, lubricant and antiwear.

2. Experimental section

2.1. Sample preparation

The n-type Si (100) wafers, the stainless steel (AISI 201) slices and the Al foils with the low surface roughness were applied as

* Corresponding author at: State Key Laboratory of Solid Lubrication, Lanzhou Institute of Chemical Physics, Chinese Academy of Sciences, Lanzhou 730000, China.
** Corresponding author.
E-mail addresses: wetrainzjy@163.com (J. Zheng), jyhao@licp.cas.cn (J. Hao).
[1] These authors contributed equally to this work.

http://dx.doi.org/10.1016/j.apsusc.2016.09.153
0169-4332/

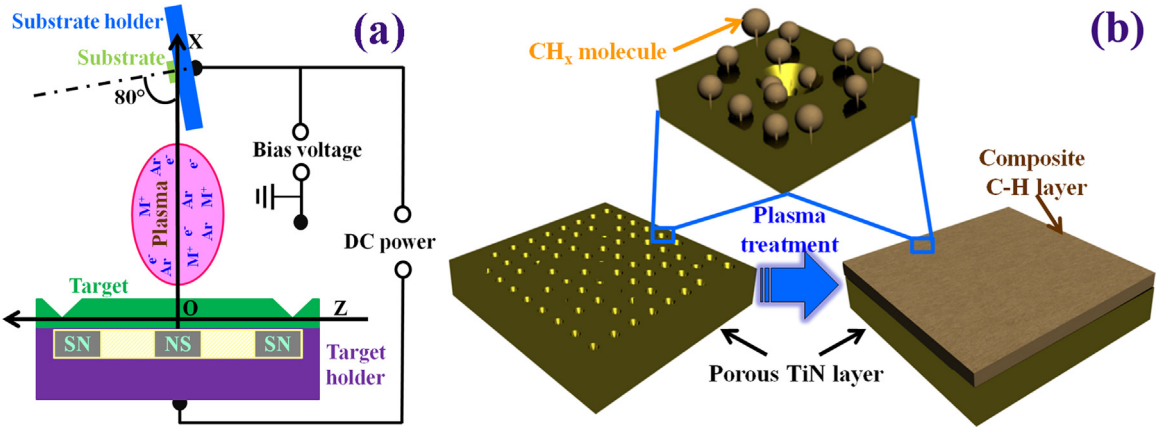

Fig. 1. (a) Schematic diagram of the deposition configuration, (b) schematic illustration for the preparation of CTF during CH_4 plasma treatment.

Table 1
Preparation parameters of the TiN porous layer and the carbon nanohoops.

Layer	Target power (W)	Target	Bias voltage (V)	Time (min)	Pressure (Pa)	Ar flow rate (sccm)	N_2 flow rate (sccm)	CH_4 flow rate (sccm)
TiN	1200	Ti	−100	40	0.4	20	8	0
Carbon nanohoops	0	Ti	−1100	80	4.0	0	0	90

the substrates. Firstly, TiN porous layer was deposited using a dcMS system (SKY Technology Development Co. Ltd., JS-650) with glancing angle [13,14] to sputter planar rectangular metal titanium target (purity >99.5 wt.%) in mixed atmosphere of Ar (99.99%) and N_2 (99.99%) at room temperature. The schematic diagram of the deposition configuration is shown in Fig. 1a. Using a load-lock system, the base pressure of the deposition chamber was kept at 8.0×10^{-4} Pa. Thereafter, the power was charged on the metal target with injection of mixed gas and the TiN porous layer/film was fabricated by oblique angle deposition with the angle of 80°. After deposition, the CH_4 plasma treatment was conducted by the glow discharge in the deposition chamber, as described in Fig. 1b. Details of the preparation parameters of the TiN porous layer and the carbon nanohoops are listed in Table 1.

2.2. Film characterization

The chemical composition of the film surface was analyzed by X-ray photoelectron spectroscopy (XPS) with monochromated Al Kα radiation at the pass energy of 29.4 eV. X-ray diffraction (XRD) was employed to characterize the crystalline structure of the films using a Philips X'perts diffractometer with grazing angle made. In order to determine the composition and structure of carbon nanohoops, a HR800 Raman microscope instrument was used with 532 nm Ar ion laser and a resolution of 2 cm^{-1}. The root-mean-square (RMS) roughness of the films was obtained by atomic force microscopy (AFM) in tapping mode. Unless stated otherwise, the RMS roughness was calculated three times at a different spot with $2 \times 2\ \mu m^2$ area. To observe the microstructure of the films, field emission scanning electron microscopy (FESEM, JSM-6701F) and high-resolution transmission electron microscopy (HRTEM, Tecnai G2 F20 S-Twin) were applied to detect the surface and cross section of the films.

The isotropic biaxial stress in the film was acquired from the radius of curvature technique which compared the curvatures of the bare silicon substrates and substrates coated with a film. The stress was given by Stoney's equation [15]:

$$\sigma = -\frac{E_s h_s^2}{6(1-\upsilon_s)h_f}\left(\frac{1}{R_a}-\frac{1}{R_b}\right) \quad (1)$$

where E_s and υ_s are elastic modulus and Poisson's ratio of the substrate, h_s and h_f the thickness of the substrate and film, R_a and R_b the spherical radius of curvature after and before preparation. The E_s, υ_s and h_s of n-Si (100) set as 131 GPa, 0.2782 and 625 μm, respectively. The film thickness (h_f) was measured by FESEM. Before and after preparation, the radius of curvature of each Si wafer was monitored by Micro XAM-3D Surface Profile. For each wafer, five measurements were carried out.

The hardness and elastic modulus were performed by using a nanoindenter (Nano Indenter XT) with a Berkovich diamond tip. The mean value of the hardness and elastic modulus of the film was obtained from the loading-unloading curves over 3 times. The indentation depth was about 10% of the film thickness in order to reduce the influence of substrate materials.

The tribological behaviors of the films were evaluated by UMT-2MT tribometer (Center for Tribology) at room temperature about 20 ± 5 °C and humidity of $40 \pm 5\%$. In the sliding process, the Si_3N_4 balls (hardness of ~90 HRA and elastic modulus of ~400 GPa) were as the counterparts with a diameter of 3 mm. The tests were done at a sliding speed of 600 rpm and a sliding stroke of 5 mm. The normal load was 3.0 N, corresponding to a theoretical initial Hertzian contact pressure of ~1.6 GPa. After the tribological tests, the 3D surface profiler was used to observe the depth and width of the wear track and calculate the wear volume. Then the wear rate (W) was figured up with the following equation:

$$W = \frac{V}{ND} \quad (2)$$

where V, N and D denote as the wear volume, normal load and the sliding distance, respectively.

2.3. First-principles calculations

In order to demonstrate the frictional mechanism of the carbon nanohoops, the separation work (W_{sep}) between the carbon nanohoop and Si_3N_4 materials was acquired through first-principles calculations. All calculations here were based on the Density Functional Theory (DFT) and were performed by using the Vienna Ab initio Simulation Package (VASP) [16]. The Perdew-Burke-Ernzerhof (PBE) generalized gradient approximation (GGA) was used to cope with the exchange-correlation functional, and the projector augmented wave (PAW) method was applied to treat the valence electron-ion interaction [17,18]. It should be noticed

that the W_{sep} cannot be calculated based on an interfacial model due to the presence of amorphous C—H material. While based on an adsorption model, the bonding strength between carbon nanohoop and Si_3N_4 materials can be calculated, and then the W_{sep} can be estimated by the bonding strength per square angstrom. A carbon nanohoop unit with 6 benzenes was taken as the adsorbate, and Si_3N_4 (001) surface was taken for the substrate of the adsorption model. Considering the low density of the C—H material, large supercells (about 15 Å × 15 Å × 27 Å) for the adsorption model were built. For all the calculations, an energy cutoff of 400 eV and 2 × 2 × 1 K-point Monkhorst–Pack grid were used.

3. Results and discussion

To confirm the phase constituents of the films, XRD patterns are recorded in Fig. 2a. Single peak matching well with the (002) plane of the cubic TiC_yN_x phase was found in CTF, while the diffraction peak of TF shifted to higher angles. It is well-known that the C atoms as interstitial impurities insert into the TiN lattice giving rise to the expansion of host lattice [19]. In addition, to further judge the reaction of CH_4 plasmas and TiN crystals, XPS spectrum of C 1s of TiN porous film treated by 2 min CH_4 plasma is provided in the inset of Fig. 2a. After deconvolution with a Lorentzian-Gaussian distribution function is implemented, the C 1s spectrum of the film shows four peaks at 481.9, 284.2, 285.1 and 287.7 eV, which are assigned to Ti—C, sp^2—C, sp^3—C and N—C bonds, respectively [20–23]. Besides, the extra peak at 284.8 eV is ascribed to the carbonaceous contaminant absorbed in the film surface [24]. In the light of these results, it can be asserted that the energy of CH_4 plasmas is enough high to react with the TiN for the formation of TiCN. Meanwhile, as regards the presence of sp^2—C and sp^3—C, it is rational reason that the CH_4 plasma treatment can create some carbon materials by the interaction of CH_x ions. Raman spectroscopy is a powerful tool to identify and characterize all the members of the carbon family, both at the lab- and at mass-production scale [25,26]. Fig. 2b displays the Raman spectrum of CTF from 750 cm^{-1} to 3500 cm^{-1}. To analyze the evolution of carbon bonds, the Raman spectrum of CTF from 950 cm^{-1} to 1750 cm^{-1} is deconvoluted into four peaks. Firstly, one can clearly find that the spectrum have a strong peak located at around 1550 cm^{-1}, namely G peak, which extremely depends on the bond stretching of all pairs of sp^2—C atoms in rings and chains. Additionally, a peak at 1395 cm^{-1} should be associated with the breathing modes of sp^2—C atoms in the rings only, habitually called as D peak [27]. Another peak at 1200 is related to the bending motions of C—H bonds in the benzene planes [28] or trans-polyacetylene segments[29]. Then, it must be pointed out that a weak peak near 1000 cm^{-1} is similar to the Raman mode of carbon nanohoops (or [n]cycloparaphenylene molecules) [10]. This mode has its counterparts in symmetric benzene ring breathing with constant C—H lengths (~990 cm^{-1}) [28]. Finally, the single, small and broad peak at approximate 840 cm^{-1} can pertain to the bending of the C—H bonds perpendicular to the benzene planes. Usually, the characteristic Raman modes of CNTs and carbon nanohoops mainly include the radial breathing mode (RBM, 100–300 cm^{-1}) [28], as recorded in the insert of Fig. 2b. Thereinto, four peaks at 130.0, 142.3, 152.8 and 162.4 cm^{-1} should belong to the RBM of carbon nanohoops with different numbers of benzene ring. However, unlike the CNTs, the RBM of carbon nanohoops is a weak signature Raman mode. The remaining peak around 110 cm^{-1} is mostly characterized by the change of the torsion angles of the benzene unites [28]. In addition, the second-order features of Raman spectrum exhibit two distinct groups of bands. The weak feature observed at ~2740 cm^{-1} is assigned as the overtone of the D mode, also denoted as 2D or G' [30]. The spectrum is dominated by the stronger feature near 3000 cm^{-1}, which can be allocated to the C—H bond stretching or the composed of multiple modes of benzene and carbon nanohoop [28,31]. As a result, the carbon nanohoops are created during CH_4 plasma treatment. Regarding the C—H vibrational modes, Fourier transform infrared spectroscopy (FTIR) was used to survey the multilayer film, as given in the SI. Two IR peaks for CTF appeared at ~2850 and ~2920 cm^{-1}. In the previous investigation, it has been uncovered that the stretching of sp^3—CH_2 and —CH results in the two IR mode [32]. Summarizing these results, we can formulate the production of carbon nanohoops, amorphous carbon and TiCN during CH_4 plasma treatment. Frankly, the mixture of carbon nanohoops and amorphous carbon is inevitable to generate a composite C—H layer.

FESEM image of fractured cross-section of CTF is exhibited in Fig. 2c. The thickness of the multilayer film was about 1440 nm, which made up of ~330 nm composite C—H layer and ~1100 nm TiN layer. Obviously, the TiN layer showed tilted columnar structure with an angle (β = 25.3°) between the column's axis and the substrate normal, while the composite C—H layer was featureless and smooth. The existence of obscure interface between tilted columnar crystals can be hypothesized the composite C—H permeated into their gaps by plasma treatment. It should be demonstrated in the inset (down) of Fig. 2c that the surface of TiN layer derived from TF was rough with a certain amount of cracks and holes, as being analogous to previous reports by glancing angle deposition [33,34]. Correspondingly, the composite C—H layer on the top of CTF owned flat surface with a considerably low value of RMS (~1.16 nm). HRTEM study was done on the multilayer film with much attention devoted to the interface between the TiN porous layer and the composite C—H layer, as offered in Fig. 2d. The contact area of the two layers (marked by red dash line) showed like the structure of the borehole case-in-place pile, which can enhance effectively their adhesion. The spacing of the lattice fringes was around 0.241 nm in the TiN porous layer, in line with the (002) plane of TiC_yN_x phase. Furthermore, one can clearly see that a small quantity of C—H lay in the adjacent lattice fringes, affirming convincingly the preceding hypothesis. Besides, some cross-linked nano-structures were observed in the magnification image of the composite C—H layer. The nano-structure mates nicely the results of Raman spectrum of CTF, namely the presence of carbon nanohoops. On basis of the characterization of composition and structure, CTF is composed of the TiN porous layer as a framework, the composite C—H layer containing carbon nanohoops, and the thin TiCN interlayer between the first two layers.

To the best of our knowledge, we used a physical route to synthesize carbon nanohoops for the first time. The generation and geometry of carbon nanohoops via CH_4 plasma treatment is briefly depicted in Fig. 3. During plasma treatment, a large amount of charged CH_x species are produced by bias voltage. Owing to high work pressure (4.0 Pa), the charged CH_x species are easier to collide with each other and merge into the charged multiple hydrocarbon molecules (C_yH_x). Thereinto, charged C_2H_2 as an incredibly fractional C_yH_x species can interact with itself to yield charged benzene like the cyclotrimerization of acetylene in chemical method [35,36]. This rearrangement is a prototypical thermally allowed (2 + 2 + 2) cycloaddition where three acetylenic π-bonds are converted into carbon–carbon σ-bonds to render the archetype of aromaticity, benzene. The newly charged benzene generally has a high reactivity in charged sit. When two charged benzene meet in the plasma group accidentally, a tandem Suzuki coupling/macrocyclization sequence [37] will be supposed to occur in a straightforward manner. Mechanistically, the reaction is envisioned to proceed via the other charged benzene until the formation of the strained carbon nanohoop. Especially noteworthy is the electron transfer in these reactions which generates stabilized radical intermediate [10]. However, computational studies have revealed that the strain energy of the carbon nanohoops increases with decreas-

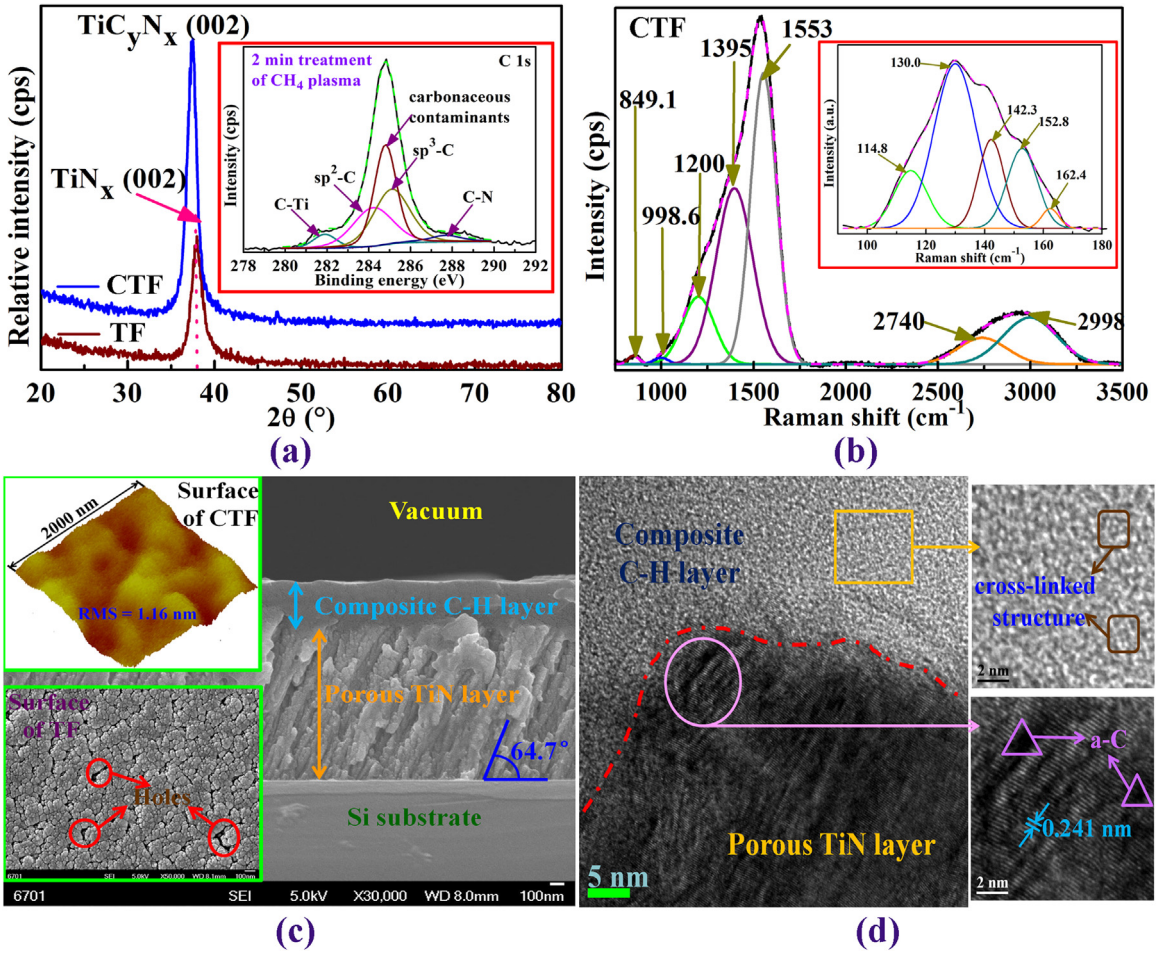

Fig. 2. (a) XRD patterns of CTF and TF (the inset shows XPS spectrum of C 1s of TiN porous film treated by 2 min CH_4 plasma), (b) Raman spectrum of CTF from 750 cm^{-1} to 3500 cm^{-1} (the inset is Raman spectrum of CTF in short Raman shift), (c) FESEM image of fractured cross-section of CTF (the insets are surface morphology of CTF (up) and TF (down), respectively), (d) cross-sectional HRTEM image of CTF (the insets correspond to the magnification images of the marked areas).

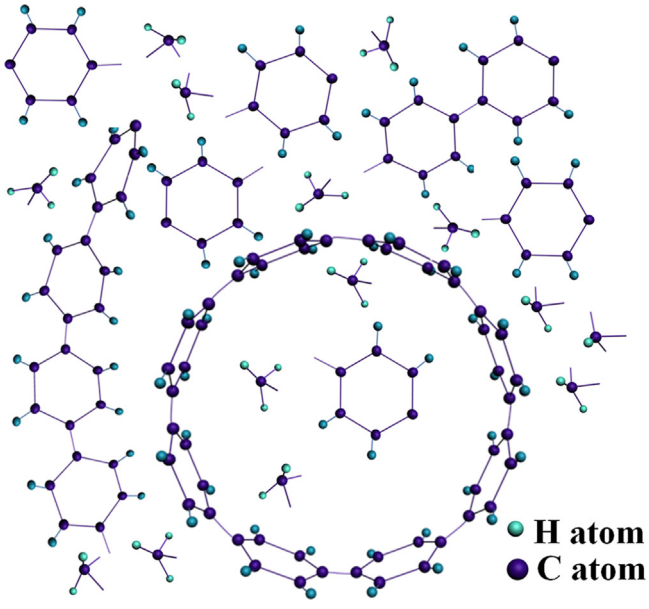

Fig. 3. Diagram illustrating of the generation and geometry of carbon nanohoops.

ing the number of benzene (n) [1,11]. For example, the strain energy of carbon nanohoops with $n = 20$ and 6 is about 29 and 97 kcal mol^{-1}, respectively. Because of the increase of strain energy, the smaller carbon nanohoops are extremely challenging synthetic targets. Herein, based on the size of cross-linked nano-structure in HRTEM image and the former research [38], we report the carbon nanohoops with $n = 8$–12 by using CH_4 plasma treatment.

The nano-indentation tests are useful to understand the evolution of mechanical properties of thin film and to evaluate the fate of thin film applied in engineering since the deformation resistant is obtained. Fig. 4a illustrates the typical loading-unloading curves of CTF. It is worthy to note that there were a small hysteresis and a low residual indentation depth (d_{res}) in these curves. The elastic recovery (W_e) of the film was calculated by using the following equation [39]:

$$W_e = \frac{d_{max} - d_{res}}{d_{max}} \times 100\% \quad (3)$$

where d_{max} is the maximum indentation depth. According to the data listed in Fig. 4a, all values of W_e of CTF were more than 60%, turning out that elastic or reversible deformation is predominant during indentation process. Moreover, mechanical properties of CTF were compared to that of TF, as presented in Fig. 4b. The hardness (H), the effective elastic modulus (E^*) and the ratio of hardness and effective elastic modulus (H/E^*) of CTF were around 30.8 GPa, 185.4 GPa and 0.166, respectively, which were evidently higher

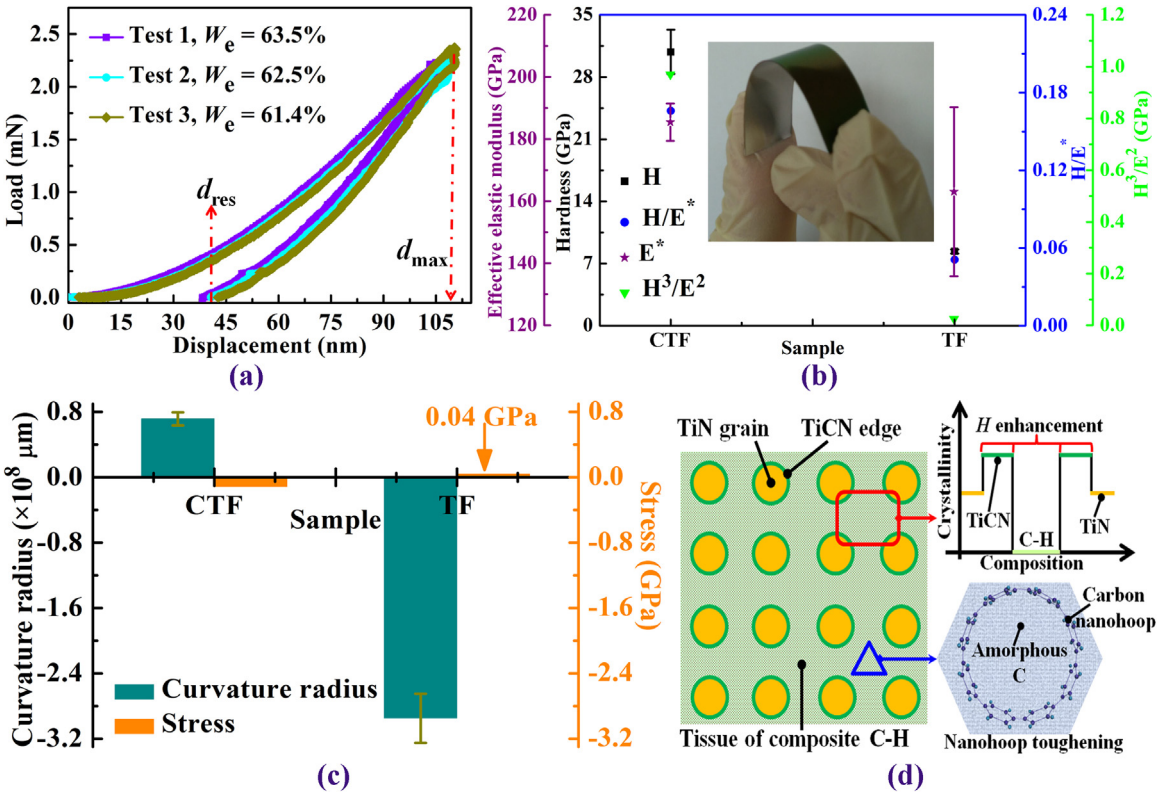

Fig. 4. (a) Typical loading-unloading curves of CTF, (b) the relative specification of mechanical properties for CTF and TF (the inset is the photograph of CTF after curving), (c) the curvature radius and the internal stress of CTF and TF, (d) schematic diagram of the mechanism of hardening and toughening of CTF.

than those of TF. Here, the interrelationship of the effective elastic modulus and the elastic modulus E is as below:

$$E^* = \frac{E}{1-\upsilon^2} \tag{4}$$

where υ is the Poisson's ratio of the film (0.25 given in nanoindentation tests). In fact, the common features of flexible hard films have been identified by Musil [12]: (1) a high hardness $H > 20$ GPa, (2) a high ratio $H/E^* \geq 0.1$, (3) a high elastic recovery $W_e \geq 60\%$, (4) the dense microstructure and the compressive macrostress ($\sigma < 0$). Fig. 4c shows the curvature radius and the internal stresses of the films. Obviously, the stress value (−0.12 GPa) of CTF was negative, and its absolute value was higher than that of TF (0.04 GPa). As a general rule, the compression stress of the films is closely bound up with the dense microstructure (Fig. 2d). Therefore, as visualized in the inserted image of Fig. 2b, the multilayer film grown on Al foil shows a good flexibility, resisting to cracking in bending. Furthermore, it is known that the H^3/E^2 ratio as a key parameter always predicts the ability of a film to resist mechanical degradation and failure [40]. The value of H^3/E^2 ratio of CTF (~0.97 GPa) in Fig. 4b is considerably higher than that of TF (~0.03 GPa). As a result, CTF should possess a superior wear resistance due to a good plastic deformation resistance with the high H^3/E^2. The details will be discussed in the later section.

From the analysis of structure and composition, the possible mechanisms for high hardness and toughness of CTF are proposed as the following, which is schematically exhibited in Fig. 4d. For the increase of hardness, two processes would occur: (i) C ions react with TiN grains to compound the TiCN grains over the surface of TiN layer during CH_4 plasma treatment, (ii) the composite C—H fills in the holes of TiN layer and permeates in the gaps of the columnar crystals via plasma interaction [41]. Accordingly, there are at least two types of nanostructures that result in the enhanced hardness of CTF: nanograins surrounded by very thin tissue of the composite C—H and the mixture of nanograins with TiN and TiCN phases [42]. These nanostructures increasing the hardness possess frequently the nanosize bilayers or transition regions where the structure changes from crystalline to amorphous or from one crystalline material to another, as displayed in Fig. 4d. From this figure is seen that to every transition region corresponds a creation of hard phase/soft phase nanocomposite, for instance TiCN/TiN and TiCN/composite C—H. To obtain high hardness in nanocomposite films, usually plastic deformation is designed to be prohibited, and dislocation movement and grain boundary sliding are prevented, thus causing a loss in ductility [43]. However, in our work, a high toughness in CTF results from the presence of carbon nanohoops. As we all know, carbon nanohoops, or [n] cycloparaphenylene molecules, represent the shortest possible subunit of an (n, n) armchair carbon nanotube [10]. The carbon nanohoops like carbon nanotubes (E = ~1.0 TPa) should be ideal reinforcing fibres for composites. One can conjecture that the carbon nanohoops can effectively lead to the phenomena of crack deflection and crack bridging to improve the toughness. Future work is planned to examine the toughening mechanisms of carbon nanohoop in detail.

Fig. 5a presents coefficient of friction (COF) of CTF as a function of sliding cycles. The COF of CTF firstly reached to a very low state (<0.036) after a very short running-in period (around 300 sliding cycles), and then maintained in a stable condition (~0.027) for the rest of sliding cycles. The insets of Fig. 5a summarize the 3D image (left) and the cross sectional profile (right) of wear scar detected through a 3D surface profiler after 18000 sliding cycles. It is expected that the wear scar on the film surface was very shallow and narrow, and its depth was less than 80 nm after 18000 sliding cycles. In view of the condition and Eq. (2), the wear rate of CTF is 1.83×10^{-8} mm^3 N^{-1} m^{-1}, such small value in according with the high H^3/E^2 ratio. Additionally, the formation of carbonaceous transfer layer was nearly avoiding on the counterfaces, as

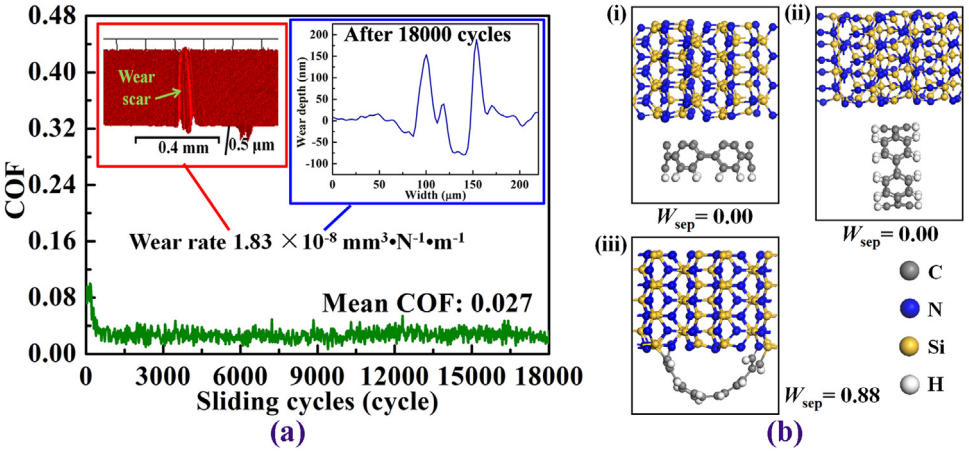

Fig. 5. (a) COF curve of CTF against Si_3N_4 ball (the insets are the 3D image (left) and the cross sectional profile (right) of wear scar, respectively), (b) armchair (i), basal (ii), and zigzag (iii) type adsorption structures for the carbon nanohoop/Si_3N_4 (001). The W_{sep} values in J m^{-2} are shown near the respective structures.

shown in SI. On the other hand, CTF sliding against Al_2O_3 ball had a higher COF (>0.05, depicted in SI) in comparison to against Si_3N_4 ball. Consequently, it can be believed that the outstanding tribological behaviors stem from intrinsically weak-interacting sliding interfaces between the composite C—H layer and the Si_3N_4 ball. Meanwhile, as described in SI, TF sliding against Si_3N_4 ball showed a poor lubricating property. However, when the composite C—H layer was directly deposited on a dense TiN layer with columns perpendicular to the film/substrate interface, the film provided a bad tribological performance (seen in SI) because of the weak anchoring strength between the composite C—H layer and the dense TiN layer. On the basis of the above results, the composite multilayer film clearly incorporates into flexible, hard, lubricant and antiwear effects.

Determining the adhesion of the film/Si_3N_4 interfaces can contribute to clarifying the impacts of the composite C—H on the tribological properties of CTF. First-principles calculations of W_{sep} are a useful and convenient assessment of the interface adhesion strength. Importantly, a large W_{sep} value for Si_3N_4/amorphous C—H couple (3.68 J m^{-2}), which indicates the strong chemical bonds existing in the interface of the couple and the formation of transfer layer, has been reported by other researchers [44]. However, the previous calculation is in contrast to the tribological behaviors in our present work. Hence, we employ first-principles calculations to study adhesion between carbon nanohoop and Si_3N_4 aiming to gain a fundamental understanding of the frictional mechanism of CTF. Adsorption structures and separation works of carbon nanohoop/Si_3N_4 (001) are shown in Fig. 5b. These structures include all possible bonding structures, namely armchair, basal and zigzag type, between the carbon nanohoop unit and Si_3N_4 (001) material. It should be stated briefly that the zigzag type bonding exists only in case of C—H unites fracture. There are strong covalence C—N and C—Si bonds forming between carbon nanohoop and Si_3N_4. While for other bonding types, their separation work is negligible. This implies that the zigzag edge states of carbon nanohoop are more active bonding to the Si_3N_4 material. Exhilaratingly, due to the low density of active sites the W_{sep} value between carbon nanohoop and Si_3N_4 is still small (not more than 0.88 J m^{-2}), which is the reason why the COF of the composite multilayer film is rather low.

4. Conclusion

In conclusion, carbon nanohoops were prepared by CH_4 plasma treatment at low temperature without using organic reagents. The carbon nanohoops as toughening and lubricant agents significantly modified the mechanical and tribological properties of TiN porous films. The TiN porous films with carbon nanohoops simultaneously showed flexible, hard, lubricant and antiwear effects. The toughening lay crucially on the contribution role of the natural characters of carbon nanohoop. The weak-interacting sliding interfaces between carbon nanohoop/Si_3N_4 ball certified by first-principles calculations leaded to the low COF of the TiN porous films with carbon nanohoops.

Acknowledgements

The authors are grateful to the National Basic Research Program of China (No. 2013CB632302), the National Natural Science Foundation of China (NSFC, No.: 51375471), and the Independent Innovation Plan Foundations of Qingdao City of China (No. 16-5-1-97-jch).

Appendix A. Supplementary data

Supplementary data associated with this article can be found, in the online version, at http://dx.doi.org/10.1016/j.apsusc.2016.09.153.

References

[1] T. Iwamoto, Y. Watanabe, Y. Sakamoto, T. Suzuki, S. Yamago, J. Am. Chem. Soc. 133 (2011) 8354–8361.
[2] R. Satio, G. Dresselhaus, M.S. Dresselhaus, Physical Properties of Carbon Nanotubes, Imperial College Press, London, 1998.
[3] M.J. O'Connell, Carbon Nanotubes: Properties and Applications, Taylor & Francis, Boca Raton, FL, 2006.
[4] P.J.F. Harris, Carbon Nanotube Science: Synthesis, Properties and Applications, Cambridge University Press, Cambridge, 2009.
[5] M.F. Yu, O. Lourie, M.J. Dyer, K. Moloni, T.F. Kelly, R.S. Ruoff, Science 287 (2000) 637–640.
[6] M.B. Nardelli, B.I. Yakobson, J. Bernholc, Phys. Rev. Lett. 81 (1998) 4656–4659.
[7] G.D. Zhan, J.D. Kuntz, J. Wan, A.K. Mukherjee, Nat. Mater. 2 (2003) 38–42.
[8] H. Takaba, H. Omachi, Y. Yamamoto, J. Bouffard, K. Itami, Angew. Chem. Int. Ed. 48 (2009) 6112–6116.
[9] R. Friederich, M. Nieger, F. Vogtle, Chem. Ber. 126 (1993) 1723–1732.
[10] R. Jasti, J. Bhattacharjee, J.B. Neaton, C.R. Bertozzi, J. Am. Chem. Soc. 130 (2008) 17646–17647.
[11] J.L. Xia, R. Jasti, Angew. Chem. Int. Ed. 51 (2012) 2474–2476.
[12] J. Musil, RSC Adv. 5 (2015) 60482–60495.
[13] Y. Li, T. Sasaki, Y. Shimizu, N. Koshizaki, J. Am. Chem. Soc. 130 (2008) 14755–14762.
[14] Z. Huang, K.D. Harris, M.J. Brett, Adv. Mater. 21 (2009) 2983–2987.
[15] J.Y. Zheng, J.Y. Hao, X.Q. Liu, Q.Y. Gong, W.M. Liu, Appl. Surf. Sci. 280 (2013) 764–771.
[16] G. Kresse, J. Furthmuller, Phys. Rev. B 54 (1996) 11169–11186.
[17] J.P. Perdew, K. Burke, M. Ernzerhof, Phys. Rev. Lett. 78 (1997) 1396.

[18] P.E. Blochl, Phys. Rev. B 50 (1994) 17953–17979.
[19] J. Lin, J.J. Moore, B. Mishra, M. Pinkas, W.D. Sproul, Acta Mater. 58 (2010) 1554–1564.
[20] J. Meng, J. Lu, J. Wang, S. Yang, Mater. Sci. Eng.: A 418 (2006) 68–76.
[21] P.A. Brühwiler, A.J. Maxwell, C. Puglia, A. Nilsson, S. Andersson, N. Mårtensson, Phys. Rev. Lett. 74 (1995) 614–617.
[22] J.F. Morar, F.J. Himpsel, G. Hollinger, J.L. Jordan, G. Hughes, F.R. McFeely, Phys. Rev. B 33 (1986) 1340–1345.
[23] B.C. Holloway, O. Kraft, D.K. Shuh, M.A. Kelly, W.D. Nix, P. Pianetta, S. Hagström, Appl. Phys. Lett. 74 (1999) 3290–3292.
[24] S. Akhter, X.L. Zhou, J.M. White, Appl. Surf. Sci. 37 (1989) 201–216.
[25] M.S. Dresselhaus, A. Jorio, A.G. Souza Filho, R. Saito, Philos. Trans. R. Soc. A 368 (2010) 5355–5377.
[26] T.C. Dinadayalane, J. Leszczynski, Struct. Chem. 21 (2010) 1155–1169.
[27] G. Irmer, A. Dorner-Reisel, Adv. Eng. Mater. 7 (2005) 694–705.
[28] H. Chen, M.R. Golder, F. Wang, R. Jasti, A.K. Swan, Carbon 67 (2014) 203–213.
[29] A.C. Ferrari, J. Robertson, Phys. Rev. B 63 (2001) 121405.
[30] D. Zhang, J. Yang, Y. Li, Small 9 (2013) 1284–1304.
[31] R. Tsu, H. J. González, C. Isaac Hernández, Solid State Commun. 27 (1978) 507–510.
[32] P.K. Chu, L. Li, Mater. Chem. Phys. 96 (2006) 253–277.
[33] J. Lintymer, J. Gavoille, N. Martin, J. Takadoum, Surf. Coat. Technol. 174–175 (2003) 316–323.
[34] D.W. Flaherty, Z. Dohnálek, A. Dohnálková, B.W. Arey, D.E. McCready, N. Ponnusamy, C.B. Mullins, B.D. Kay, J. Phys. Chem. C 111 (2007) 4765–4773.
[35] K.N. Houk, R.W. Gandour, R.W. Strozier, N.G. Rondan, L.A. Paquette, J. Am. Chem. Soc. 101 (1979) 6797–6802.
[36] R.W.A. Havenith, P.W. Fowler, L.W. Jenneskens, E. Steiner, J. Phys. Chem. A 107 (2003) 1867–1871.
[37] Z.Z. Song, H.N.C. Wong, J. Org. Chem. 59 (1994) 33–41.
[38] H. Omachi, T. Nakayama, E. Takahashi, Y. Segawa, K. Itami, Nat. Chem. 5 (2013) 572–576.
[39] J.Y. Zheng, J.Y. Hao, X.Q. Liu, Q.Y. Gong, W.M. Liu, Surf. Coat. Technol. 209 (2012) 110–116.
[40] D. Galvan, Y.T. Pei, J.T.M. De Hosson, Surf. Coat. Technol. 200 (2006) 6718–6726.
[41] J.Y. Zheng, J.Y. Hao, X.Q. Liu, Q.Y. Gong, W.M. Liu, Appl. Surf. Sci. 268 (2013) 195–203.
[42] J. Musil, Surf. Coat. Technol. 207 (2012) 50–65.
[43] S. Zhang, H.L. Wang, S.E. Ong, D. Sun, X.L. Bui, Plasma Processes Polym. 4 (2007) 219–228.
[44] L.C. Cui, Z.B. Lu, L.P. Wang, ACS Appl. Mater. Interfaces 5 (2013) 5889–5893.